Cancer Research

Drugging MYCN Oncogenic Signaling through the MYCN-PA2G4 Binding Interface

Jessica Koach[1,2], Jessica K. Holien[3], Hassina Massudi[1], Daniel R. Carter[1,4,5], Olivia C. Ciampa[1], Mika Herath[1], Taylor Lim[1], Janith A. Seneviratne[1], Giorgio Milazzo[6], Jayne E. Murray[1], Joshua A. McCarroll[1,7], Bing Liu[1], Chelsea Mayoh[1], Bryce Keenan[1], Brendan W. Stevenson[3], Michael A. Gorman[3,8], Jessica L. Bell[9], Larissa Doughty[3,8], Stefan Hüttelmaier[9], Andre Oberthuer[10,11], Matthias Fischer[10,12], Andrew J. Gifford[1,13], Tao Liu[1], Xiaoling Zhang[14], Shizhen Zhu[14], W. Clay Gustafson[2], Michelle Haber[1], Murray D. Norris[1], Jamie I. Fletcher[1], Giovanni Perini[6], Michael W. Parker[3,8], Belamy B. Cheung[1,4,15], and Glenn M. Marshall[1,4,16]

Abstract

MYCN is a major driver for the childhood cancer, neuroblastoma, however, there are no inhibitors of this target. Enhanced MYCN protein stability is a key component of MYCN oncogenesis and is maintained by multiple feedforward expression loops involving MYCN transactivation target genes. Here, we reveal the oncogenic role of a novel MYCN target and binding protein, proliferation-associated 2AG4 (PA2G4). Chromatin immunoprecipitation studies demonstrated that MYCN occupies the PA2G4 gene promoter, stimulating transcription. Direct binding of PA2G4 to MYCN protein blocked proteolysis of MYCN and enhanced colony formation in a MYCN-dependent manner. Using molecular modeling, surface plasmon resonance, and mutagenesis studies, we mapped the MYCN–PA2G4 interaction site to a 14 amino acid MYCN sequence and a surface crevice of PA2G4. Competitive chemical inhibition of the MYCN–PA2G4 protein–protein interface had potent inhibitory effects on neuroblastoma tumorigenesis *in vivo*. Treated tumors showed reduced levels of both MYCN and PA2G4. Our findings demonstrate a critical role for PA2G4 as a cofactor in MYCN-driven neuroblastoma and highlight competitive inhibition of the PA2G4-MYCN protein binding as a novel therapeutic strategy in the disease.

Significance: Competitive chemical inhibition of the PA2G4–MYCN protein interface provides a basis for drug design of small molecules targeting MYC and MYCN-binding partners in malignancies driven by MYC family oncoproteins.

Introduction

The MYC oncoproteins (MYCN, MYC, and MYCL) are short-lived transcription factors that are overexpressed or deregulated in more than half of all human cancers, making them important therapeutic targets. However, the design of MYC inhibitors has been hampered by the lack of globular functional MYC domains or deep protein "pockets" for drug binding. Moreover, MYC inhibitors carry a heightened potential for side-effects due to the dependency of most normal cells on transient MYC expression at entry into the cell cycle.

Neuroblastoma is the most common solid malignancy in early childhood and advanced disease accounts for a

[1]Children's Cancer Institute Australia for Medical Research, Lowy Cancer Research Centre, UNSW Sydney, Kensington, New South Wales, Australia. [2]Department of Pediatrics, Helen Diller Family Comprehensive Cancer Center, University of California, San Francisco, California. [3]ACRF Rational Drug Discovery Centre, St. Vincent's Institute of Medical Research, Fitzroy, Victoria, Australia. [4]School of Women's & Children's Health, UNSW Sydney, Randwick New South Wales, Australia. [5]School of Biomedical Engineering, University of Technology Sydney, Australia. [6]Department of Pharmacy and Biotechnology, University of Bologna, Bologna, Italy. [7]Australian Centre for NanoMedicine, ARC Centre for Excellence in Convergent Bio-Nano Science and Technology, UNSW, Australia. [8]Department of Biochemistry and Molecular Biology, Bio21 Molecular Science and Biotechnology Institute, The University of Melbourne, Parkville, Victoria, Australia. [9]The Section for Molecular Cell Biology, Institute of Molecular Medicine, Martin Luther University of Halle, Halle, Germany. [10]Department of Pediatric Oncology and Hematology, Children's Hospital, University of Cologne, Cologne, Germany. [11]Department of Neonatology and Pediatric Intensive Care Medicine, Children's Hospital, University of Cologne, Cologne, Germany. [12]Max Planck Institute for Metabolism Research, Cologne, Germany. [13]Department of Anatomical Pathology, Prince of Wales Hospital, Randwick, New South Wales, Australia. [14]Department of Biochemistry and Molecular Biology, Cancer Center and Center for Individualized Medicine, Mayo Clinic, Rochester, Minnesota. [15]School of Life Sciences and Technology, Tongji University, Shanghai, China. [16]Kids Cancer Centre, Sydney Children's Hospital, Randwick, New South Wales, Australia.

Note: Supplementary data for this article are available at Cancer Research Online (http://cancerres.aacrjournals.org/).

J. Koach, J.K. Holien, and H. Massudi contributed equally to this article.

Corresponding Authors: Glenn M. Marshall, Centre for Children's Cancer and Blood Disorders, Sydney Children's Hospital, High Street, Randwick, NSW 2031, Australia. Phone: 612-9382-1721; Fax: 612-9382-1789; E-mail: g.marshall@unsw.edu.au; and Belamy B. Cheung, Children's Cancer Institute Australia, UNSW Sydney, PO Box 81, Randwick NSW 2031, Australia. Phone: 6102-9385-2450; Fax: 6102-9662-6584; E-mail: bcheung@ccia.unsw.edu.au

Cancer Res 2019;79:5652–67

doi: 10.1158/0008-5472.CAN-19-1112

disproportionately high mortality when compared with other childhood cancer types (1). The *MYCN* oncogene is amplified and overexpressed in 25% of patients with this embryonal childhood cancer. Furthermore, transgenic *MYCN* (TH-*MYCN*) mice develop neuroblastoma with most of the characteristics of the human disease, making neuroblastoma a model of *MYC*-driven human cancer (2, 3). MYCN drives the initiation and progression of neuroblastoma through a transcriptional program regulated by multiple protein–protein and protein–DNA interactions in malignant cells (4). Protein–protein interaction sites involving oncoproteins have become a major focus for the discovery of cancer therapeutics, whereby oncogenic signal activation or oncoprotein stability can be inhibited by competitive binding of small molecules at these protein–protein interfaces (5).

We and others have demonstrated several mechanisms by which increased MYCN protein stability acts as a necessary cofactor for *MYCN*-driven tumorigenesis (6–8). Moreover, we find that many of the proteins that directly or indirectly stabilize MYCN are themselves transactivation targets of MYCN, creating a positive feedforward regulatory loop and a therapeutic vulnerability in neuroblastoma cells (7, 8). MYC and MYCN protein stability is tightly regulated via the ubiquitin-proteasome system in normal cells, where it is an important binding target of the E3 ligase, F-box, and WD40 domain protein 7 (Fbxw7; refs. 6, 9). Fbxw7-mediated MYCN proteolysis in neuroblastoma cells can be inhibited by the Aurora A (AurA) serine-threonine kinase, which blocks binding of Fbxw7 to MYCN, or by Polo-like kinase-1 (PLK1), which induces Fbxw7 autoubiquitination (6, 10, 11). Targeting MYCN through disruption of protein interaction partners remains a highly promising approach if suitable inhibitors can be found.

The proliferation-associated 2AG4 protein (PA2G4), or ErbB3 binding protein (EBP1), binds Fbxw7, sequestering it in the cytoplasm, hence stabilizing MYC in colorectal cancer cells (12). PA2G4 is a ubiquitously expressed DNA and RNA binding protein with roles in normal embryonal muscle and neural crest cell growth (13, 14). The *PA2G4* gene transcribes two isoforms: the predominant long form, p48, and p42. Initiation of p48 translation starts at the first ATG codon, making p48 54 amino acids longer than p42. p42 translation begins at the third ATG codon, thus the protein has a truncated N-terminus, potentially resulting in its inability to translocate to the nucleus (15–17). Generally, p48 function acts as a tumor promoter whereas p42 acts as a potential tumor suppressor. Overexpression of p48 stimulates cell growth, prevents neurite outgrowth, enriches cells in S phase (15), and prevents apoptosis by interacting with AKT and HDM2 to regulate p53 (18, 19). Overexpression of p42 suppresses cell growth, initiates cell differentiation, and causes accumulation of cells in the G_1 phase of the cell cycle (20). Considerable evidence suggests that high levels of PA2G4-p48 drives cell proliferation and correlates with poor patient survival in several human cancers (16, 21). Here we show that PA2G4 is a transactivation target for MYCN in neuroblastoma cells, which directly binds to and stabilizes MYCN in a positive feedforward expression loop. Using mutant proteins and structural biologic approaches, we define a PA2G4–MYCN protein–protein interface that can be inhibited by a known PA2G4-binding compound, with significant antitumor effects *in vitro* and *in vivo*. Furthermore, we show that PA2G4 expression levels in neuroblastoma patient tumor tissues correlated with MYCN levels and poor prognosis.

Materials and Methods

Chromatin immunoprecipitation–sequencing analysis

MYCN and Input ChIP-seq fastq files were retrieved directly from the European Nucleotide Archive under the SRA accession number SRP073110 for four *MYCN*-amplified cell lines (KELLY, BE2C, NGP, and TET21N; ref. 22). Fastq files were first trimmed to remove poor quality reads and adapters (Q30 < 20, length < 20 bp) using the TrimGalore wrapper (Cutadapt/FastQC; ref. 23). Reads from the trimmed fastq's were then aligned to the reference human genome (hg38) using bowtie2 to produce sam files. Sam files were converted to the bam format and then sorted using samtools (view/sort). Duplicate reads were then removed from sorted bam files using picard tools (MarkDuplicates). Chromatin immunoprecipitation sequencing (ChIP-seq) peaks were then called using the MACS2 algorithm (callpeak; $q < 0.05$) from sorted bam files, followed by the generation of fold enrichment tracks (MYCN/Input) in bedgraph format. Peaks were called in individual cell lines and when combined as pseudoreplicates. Bedgraph files were then converted to the bigwig format using bedtools (bdg2bw). The IGV genome browser was then used to visualize fold enrichment peaks. Peaks identified by MACS2 were annotated using HOMER (annotatepeaks.pl), promoters were defined as being within −1000/+100 bp of the transcription start site (TSS). PWMtools was used to annotate canonical MYCN E-Boxes (CACGTG) across the human genome (hg38), and were visualized on IGV alongside fold enrichment tracks (24).

Cell lines

Neuroblastoma cell lines NBL-S were kindly provided by Professor Susan L. Cohn (Northwestern University, Chicago, IL), and SH-EP and SK-N-BE(2)C by Professor June Biedler (Memorial Sloan Kettering Cancer Center, New York, NY). Non-MYCN–amplified human neuroblastoma cell line SHEP MYCN-3 and SHEP-tet21N, which are genetically modified to overexpress or repress human MYCN cDNA when exposed to doxycycline, were generously supplied by Professor Jason Shohet (Texas Children's Cancer Center, Houston, TX). All other cell lines were purchased from ATCC. SK-N-AS, SK-N-DZ, SK-N-FI, SK-N-BE(2)-C, SH-EP, SH-SY5Y, LAN-1, IMR-32, NBLS, and HEK-293T were maintained in DMEM (Invitrogen, Life Technologies) with 10% FCS. CHP-134 and Kelly cells were cultured in RPMI media (Invitrogen, Life Technologies) with 10% FCS. MRC-5 and WI-38 lung fibroblast cells (ATCC) were cultured in Alpha-MEM media (Invitrogen, Life Technologies) with 10% FCS. Cell lines are passaged to a maximum of 10–15 times before being discarded. All cell lines used were authenticated by CellBank Australia, free from *Mycoplasma*, and cultured at 37°C with 5% CO_2 in a humidifier incubator.

Patient tumor sample analyses

The mRNA expression in human neuroblastoma tissues from the Cologne dataset (477 diverse patient samples) was analyzed from publically available gene expression databases (http://r2.amc.nl). Primary human neuroblastoma cDNA samples were synthesized from total RNA isolated from 40 patient tumors obtained at diagnosis from patients consecutively treated at the Sydney Children's Hospital following consenting approved by the Institutional Ethics Committee (approval number: HC12591, University of New South Wales, Sydney, Australia). The patients have given written informed consents.

Site-directed mutagenesis

Point mutations were generated by GenScript. pCMV6-PA2G4. p48-MYC Flag-tag was used as the template for the site mutagenesis of the six PA2G4 mutants. The six PA2G4 mutants used in the experiments were: mutant 1 Ser47->Ala; mutant 2 Glu50->Ala; mutant 4 Lys93->Tryptophan; mutant 5 Arg271->Ala; mutant 6 Arg272->Ala; and mutant 7 Arg281->Ala. All mutations were confirmed by direct sequencing. pShuttle-IRES-hrGFP- MYCN plasmid DNA was used as the template for the site mutagenesis of the four MYCN mutants.

ChIP assays

Preparation of DNA from SK-N-BE(2)-C and Kelly cells ($\sim 6 \times 10^7$ or more cells) for ChIP assay was performed using the Chromatin Immunoprecipitation Assay Kit (Millipore) according to the manufacturer's instructions. The shearing of DNA was performed on the Bioruptor Pico (Diagenode) with 45 sets of 30 seconds per pulse. ChIP assays were performed with 10 μg anti-MYCN antibody (Santa Cruz Biotechnology) or a control mouse IgG antibody (Santa Cruz Biotechnology). DNA from was purified using a MiniElute PCR Purification Kit (Qiagen) and eluted with 40 μL of DNase/RNase-free water. Real-time PCR was performed with primers targeting the negative control region, which was 1200 bp upstream of TSS, *PA2G4* gene promoter, PA2G4 intron 1 region, which contains two MYCN canonical E-boxes, and the ODC promoter region as a positive control. PA2G4 gene sequences containing putative MYCN-binding regions were identified by the anti-MYCN antibody, and fold enrichment was calculated by dividing the densitometric assessment of the PCR product from *PA2G4* gene promoter and PA2G4 intron 1 region by the PCR product from the negative control region, relative to input.

DNA constructs used in zebrafish experiments

Human PA2G4 was cloned into the PDONR221 gateway donor vector by BP recombination reaction. The PA2G4-PDONR221 or mCherry-PDONR221 (25) construct was combined with the other two entry clones, dβh-pDONRP4-P1R (26) and p3E-EGFPpA, as well as pDestTol2CG destination vector, using the Multisite Gateway System to generate the dβh:PA2G4 Tol2 and dβh:mCherry Tol2 transgenic constructs.

Mosaic zebrafish transgenesis and tumor watch

To mosaically overexpress PA2G4 or control mCherry in the Tg (dβh: EGFP-MYCN) transgenic fish (designated the "MYCN" transgenic line), a 1–2 nL of DNA solution containing 50 ng/μL of dβh:PA2G4 Tol2 or dβh:mCherry Tol2 DNA construct and 5 ng/μL of the Tol2 mRNA was coinjected into one-cell stage MYCN transgenic embryos. In the pDestTol2CG construct, there is a cmlc2:egfp-pA cassette. The embryos with successful integration of injected DNA constructs show the EGFP expression in the heart region. Such heart-EGFP and MYCN-EGFP double-positive embryos were sorted at day 2–5 and monitored every alternate week for EGFP/mCherry-expressing cell masses in the inter-renal gland region under fluorescence microscopy from 5 weeks onward. A Leica MZ10F Stereo fluorescence microscope was used to capture bright field and fluorescent images of tumor-bearing fish. Images were processed in Leica Application Suite X (v. 2.0.0), Adobe Photoshop, and Illustrator CC (v. 19.1.0) software. Kaplan–Meier analysis was applied to assess the rate of tumor development. Fish that died prior to evidence of external EGFP/mCherry-positive masses were censored. The log-rank statistical test was used to assess the difference between tumor onset by 11 wpf in the MYCN fish mosaically overexpressing mCherry and that in the MYCN line mosaically overexpressing PA2G4.

WS6 treatment of the MYCN transgenic zebrafish model

To further test the efficacy of WS6, another animal model, MYCN;EGFP transgenic fish, with established neuroblastomas were treated with 175.4 mg/kg of WS6 (5 μL) dissolved in vehicle (saline solution) or vehicle alone, for 7 consecutive days with a 26 G needle. After 7 days of treatment, fish were anesthetized and sacrificed for sectioning and pathology analyses. Bright-field and fluorescent images of treated tumor-bearing fish at day 1 and day 7 were taken using identical parameters on a Leica MZ10F fluorescence microscope. Images were processed with Zeiss Zen 2012, Adobe Photoshop, and Illustrator CS3 (Adobe) software. The acquired fluorescence images were quantified by measuring the EGFP-covered area using ImageJ software. Means of changes in tumor volume between WS6-treated and vehicle-treated groups were compared by Student *t* test (GraphPad prism 6). Bright-field images of hematoxylin and eosin or immunostained paraffin sections (3–5 μm each) were captured by an Olympus AX70 compound microscope equipped with an Olympus DP71 camera. Images were processed with Zeiss Zen 2012, Adobe Photoshop, and Illustrator CS3 (Adobe) software. The acquired hematoxylin and eosin or immunostained images were quantified by measuring the intensity of stained tumor using ImageJ software. Means of changes in staining intensity between WS6-treated and vehicle-treated groups were compared by Student *t* test (GraphPad prism 6).

Surface plasmon resonance binding assays

All surface plasmon resonance (SPR) was conducted on a Biacore T200 (GE Healthcare) and analyzed using the BIAevaluation software package. Wild-type, triple mutant (R271A, R272A, and S47A) and single mutant (S47A or R272A) PA2G4 protein was biotinylated using standard procedures (Thermo Fisher Scientific) and purified using a Superdex 200 10/30 GL column. The resultant proteins were captured on immobilized streptavidin, which has been coupled to a CM5 chip (GE Healthcare) via amine coupling. Final amount of biotinylated protein captured was 3500RU. Flow cell 1 was derivitized and blocked for use as a reference. MycN oligopeptides (DHKALST and GGDHKALST-GEDTL) and mutant MycN oligopeptides (DHAALST, DHAALAT, and DHKALAT) were diluted in HBS+P buffer (0.01 mol/L HEPES pH 7.4, 0.15 mol/L NaCl, and 0.005% v/v Surfactant P20) from 100 to 0.8 μmol/L in a 2-fold dilution series and injected across the chip for 60 seconds at 30 μL/minute. Experiments were conducted in duplicate at least three independent times. For the competition assay, WS6 was added at a final concentration of 10 μmol/L to the MycN dilution series. The steady-state affinities (K_d) were calculated by plotting the steady-state binding levels against the concentration.

Molecular dynamics simulations

The molecular dynamics program NAMD (27) was used to minimize the docking models of PA2G4 with MYCN oligopeptides on a TELSA K20 GPU machine (NVIDIA). Each model was initially solvated with TIP3P water using the Solvate plugin within VMD version 1.9 (28) with the rotate to minimize volume selected, the boundary reduced to 1.8, and the box padding

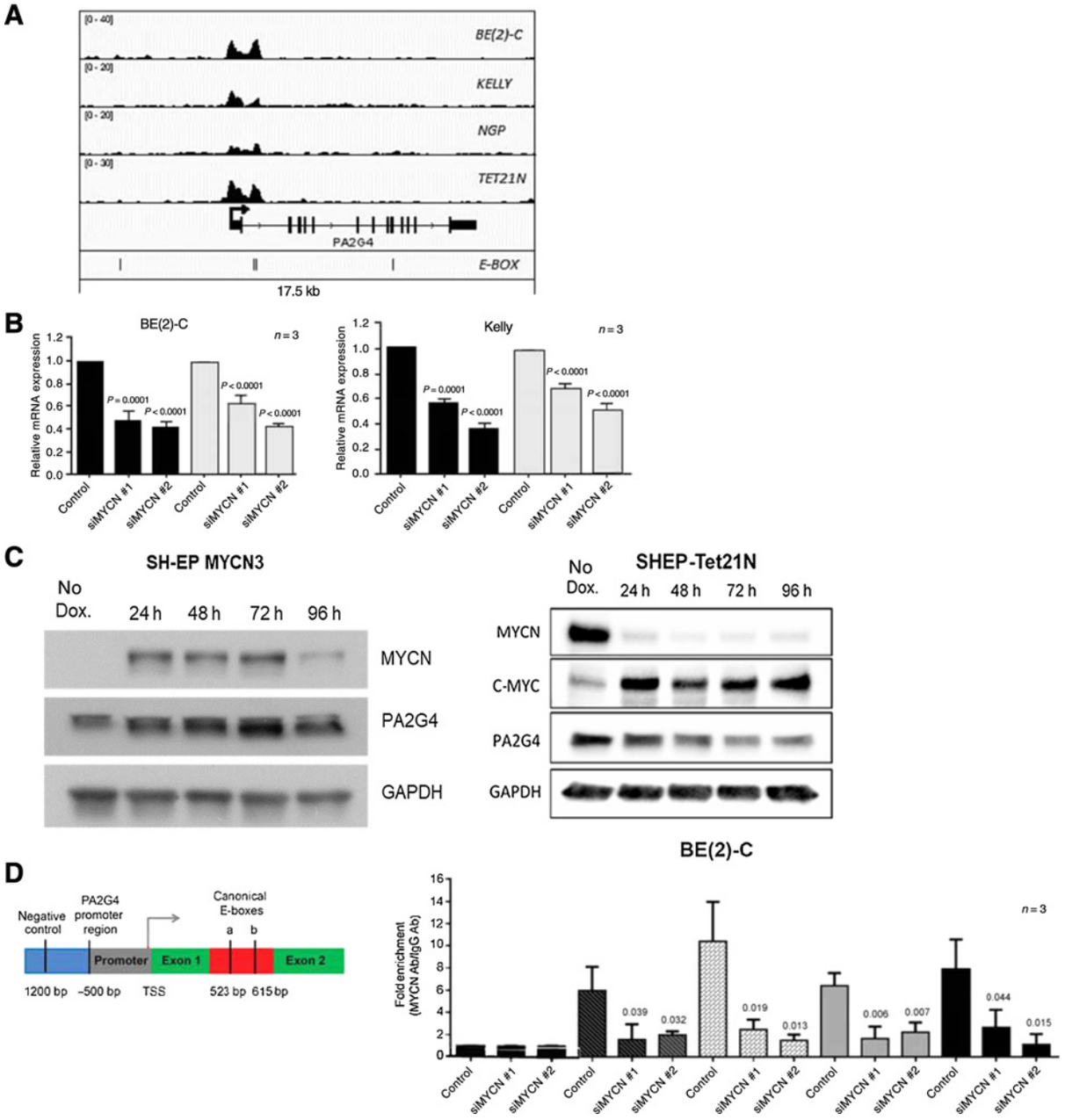

Figure 1.

PA2G4 is a MYCN transactivation target gene. **A,** Fold enrichment tracks of MYCN binding proximally to the *PA2G4* gene promoter in four MYCN-amplified neuroblastoma cell lines. The fold enrichment scale of each track is indicated in brackets. Collapsed gene structure is shown with the TSS being marked by an arrow. Canonical E-box (CACGTG) positions are annotated and the length of the plotted region is shown (kb). BE(2)-C, KELLY, NGP, and TET21N are neuroblastoma cell lines expressing MYCN. **B,** Real-time PCR analysis of MYCN and PA2G4 mRNA expression following MYCN siRNA knockdown in BE(2)-C and Kelly neuroblastoma cells. **C,** The effect of doxycycline-induced MYCN overexpression (SH-EP MYCN3), or repression (SHEP-tet21N) on PA2G4, MYCN, and MYC expression. Cells were treated with doxycycline (Dox; 1 μg/mL) for 24–48 hours. *P* values were determined by *t* test and compared with no doxycycline. **D,** ChIP assays using an anti-MYCN antibody and real-time PCR analysis with primers identifying E-Box DNA binding sites for MYCN in the *PA2G4* gene promoter (500 bp upstream of TSS) or intron 1 a and b regions of the *PA2G4* gene, with and without *MYCN* siRNA knockdown, in BE(2)-C cells. ChIP and real-time PCR analysis using primers against a region 1,200 bp upstream of TSS was used as a negative control for MYCN chromatin binding. ChIP and real-time PCR analysis using primers against the ornithine decarboxylase (*ODC1*) gene promoter region was used as a positive control for MYCN chromatin binding.

increased to 20 Å in all directions. Charges were neutralized with NaCl using the autoionize plugin within VMD version 1.9. Each structure was then minimized and equalized for 1 nanosecond under the CHARMM27 all-atom force field at 298K. Langevin dynamics were used with group pressure and langevin piston turned on. Trajectory snapshots were collected every picosecond.

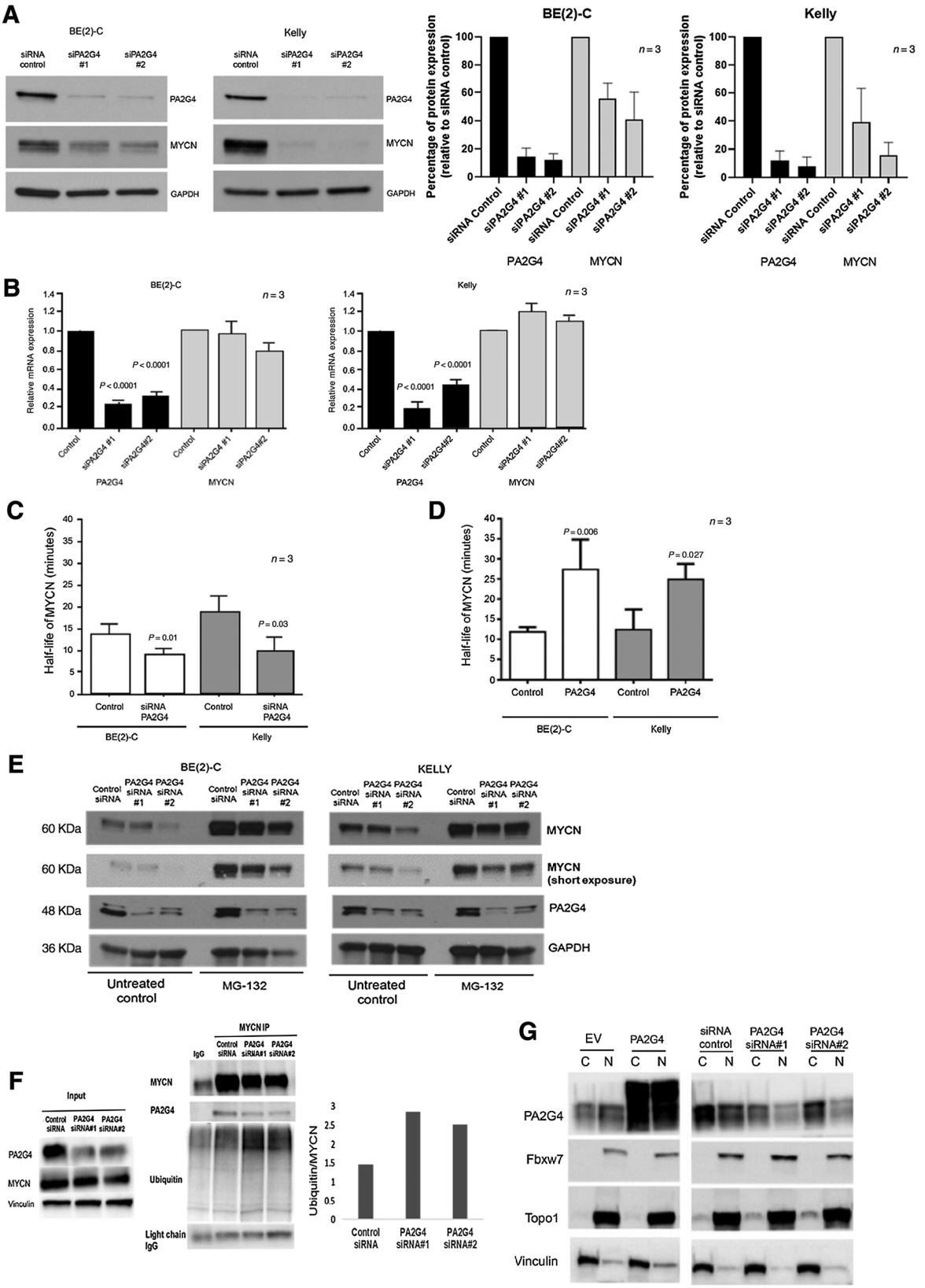

A production run was then completed 10 times for each alternate simulation (40 simulations in total) on this minimized structure for 10 nanoseconds using the same conditions as described above. Convergence was monitored by plotting root mean square deviation as a function of the entire simulation time. The first 2 nanoseconds of the production runs were calculated to be the equilibration stage, thus analyses were carried out on the final 8 nanoseconds of each production run. The H bond plugin of VMD was used to calculate the hydrogen bonds between the PA2G4 and the MYCN oligopeptide. Criteria for the formation of hydrogen bonds were that the distance between hydrogen donor (D) and hydrogen acceptor (A) atoms was less than the cut-off distance of 3.2 Å and the angle D-H-A was less than the cut-off angle of 42°. The average occupancy of the hydrogen bonds was calculated as a ratio between the number of the trajectory frames containing the hydrogen bond of interest, and the total number of frames.

In vivo murine models of PA2G4 tumorigenicity and response to WS6 treatment

SHEP PA2G4 stable–overexpressing cells, SHEP control cells expressing EV, or Kelly neuroblastoma were xenografted into BALB/c nude mice to assess the ability of PA2G4 to induce tumorigenesis. Cells were resuspended in PBS at a concentration of 6×10^6 cells per 100 μL then mixed with Matrigel (BD Biosciences) basement membrane matrix at a ratio of 1:1. The cell/Matrigel solution was kept cold on ice and 200 μL was injected subcutaneously into the dorsal flank of BALB/c nude mice (6 weeks of age). Mice were monitored for signs of tumor formation for a period of 12 weeks postinjection, and then humanely euthanized by CO_2 asphyxiation. Kelly xenografted mice were treated with the maximum tolerated dose of 70 mg/kg WS6 when the mice developed 4 mm tumor and were treated for 5 consecutive days of each week for 3 weeks or when the tumor reached an ethical limit of 1,000 mm. Tumor tissues were excised, measured, and collected for morphologic and biochemical analysis.

To assess the capability of the PA2G4 inhibitor, WS6, to delay the growth of neuroblastoma tumors, TH-*MYCN*$^{+/+}$ homozygous mice (3 weeks of age) were treated with 85 mg/kg of WS6 (100–200 μL) dissolved in DMSO, or DMSO only as control, for 5 consecutive days per week for a maximum of 3 weeks intraperitoneal injection with a 27–29 G needle. Treatment was discontinued when tumors reached 1,000 mm or 3 weeks post treatment. All mice were humanely euthanized by CO_2 asphyxiation and tumors were excised, measured, and collected for morphologic, histologic, and biochemical analysis. This study was approved by the Animal Care and Ethics Committee, UNSW Sydney (Approval number: 18/72B).

In vivo models for silencing PA2G4 expression to reduce tumor growth in mice

To assess whether PA2G4 was required for tumor growth and progression, PA2G4 expression was suppressed with highly specific siRNAs targeting PA2G4 or PA2G4.p48 gene sequences, which were delivered by nonviral and nontoxic nanoparticles synthesized by chemists at the Australian Centre for NanoMedicine, UNSW Sydney. BE(2) cells (4×10^6 in 100 μL PBS) were subcutaneously injected into the dorsal flank of BALB/c nude mice (6 weeks of age). Once tumors reached approximately 100–200 mm, mice were randomized into treatment groups to receive a local injection of nanoparticle–siRNA complexes directly into the tumor using a 0.5 mL syringe containing a 29 G needle. The solution injected into the tumor contained sterile saline with 200 μg of nanoparticles complexed to PA2G4 siRNA (40 μg) or control siRNA (40 μg; total volume 50 μL). Mice were injected once every 3 days for up to 8 injections or until the tumor reached 1,000 mm. The rate of tumor growth was measured twice weekly using digital calipers and recorded. This study was approved by the Animal Care and Ethics Committee, UNSW Sydney (Approval number: 14/152B).

Statistical analysis

All experiments included a minimum of three independent replicates. Statistical calculations were performed using GraphPad Prism 6 software. Results were compared using ANOVA among groups or two-sided unpaired *t* test for two groups and expressed as mean values with 95% confidence intervals. Graphical error bars for *in vitro* data represent the SEM, while error bars for *in vivo* data were calculated as SD. A *P* value of less than 0.05 was considered statistically significant.

Results

PA2G4 and MYCN exhibit functionally interdependent expression

We investigated whether a regulatory relationship existed between PA2G4 and MYCN expression in neuroblastoma cells with amplified and overexpressed MYCN. We first analyzed publicly available ChIP-seq data of genome-wide MYCN occupancy (22) and found that MYCN strongly bound a canonical E-Box proximal to the PA2G4 gene promoter (FE = 8.43082; $P = 2.18162E^{-83}$; $Q = 2.3877E^{-79}$; $n = 4$; Fig. 1A). We next found that MYCN-amplified neuroblastoma cells transiently transfected with MYCN-specific siRNA duplexes, displayed reduced MYCN and PA2G4 expression at the protein (Supplementary Fig. S1A), and mRNA level (Fig. 1B). Doxycycline treatment of a human neuroblastoma cell line with doxycycline-inducible MYCN

Figure 2.

PA2G4 increases MYCN protein stability. **A,** Immunoblots of PA2G4 and MYCN expression in BE(2)-C and Kelly cells following siRNA-mediated PA2G4 knockdown for 48 hours, using anti-PA2G4 and anti-MYCN antibodies. **B,** Real-time PCR quantitation of *PA2G4* and *MYCN* mRNA expression in neuroblastoma cells following *PA2G4* siRNA knockdown for 48 hours. **C** and **D,** Knockdown with *PA2G4* siRNA, or overexpression of PA2G4, in BE(2)-C and Kelly cells for 48 hours, followed by treatment with 100 μg/μL cycloheximide for up to 60 minutes. Densitometry of immunoblots was used to measure MYCN protein half-life relative to no cycloheximide. **E,** Immunoblot analysis with anti-MYCN and anti-PA2G4 antibodies against whole-cell protein lysates from BE(2)-C and Kelly cells transiently transfected with PA2G4 siRNA, then treated with 30 μmol/L MG-132 for 4 hours. **F,** Co-IP using IgG or anti-MYCN antibodies of total protein from Kelly cells transiently transfected with siRNA targeting PA2G4 for 48 hours, followed by immunoblotting with anti-PA2G4, anti-MYCN, or anti-ubiquitin antibodies. **G,** Immunoblot analysis of cytoplasmic (C) and nuclear fractions (N) from Kelly cells transiently transfected with empty vector (EV) and PA2G4 cDNA, or with siRNA targeting PA2G4 for 48 hours, probed with antibodies recognizing PA2G4 and Fbxw7. Topoisomerase and vinculin were used as markers for nuclear and cytoplasmic fractions, respectively.

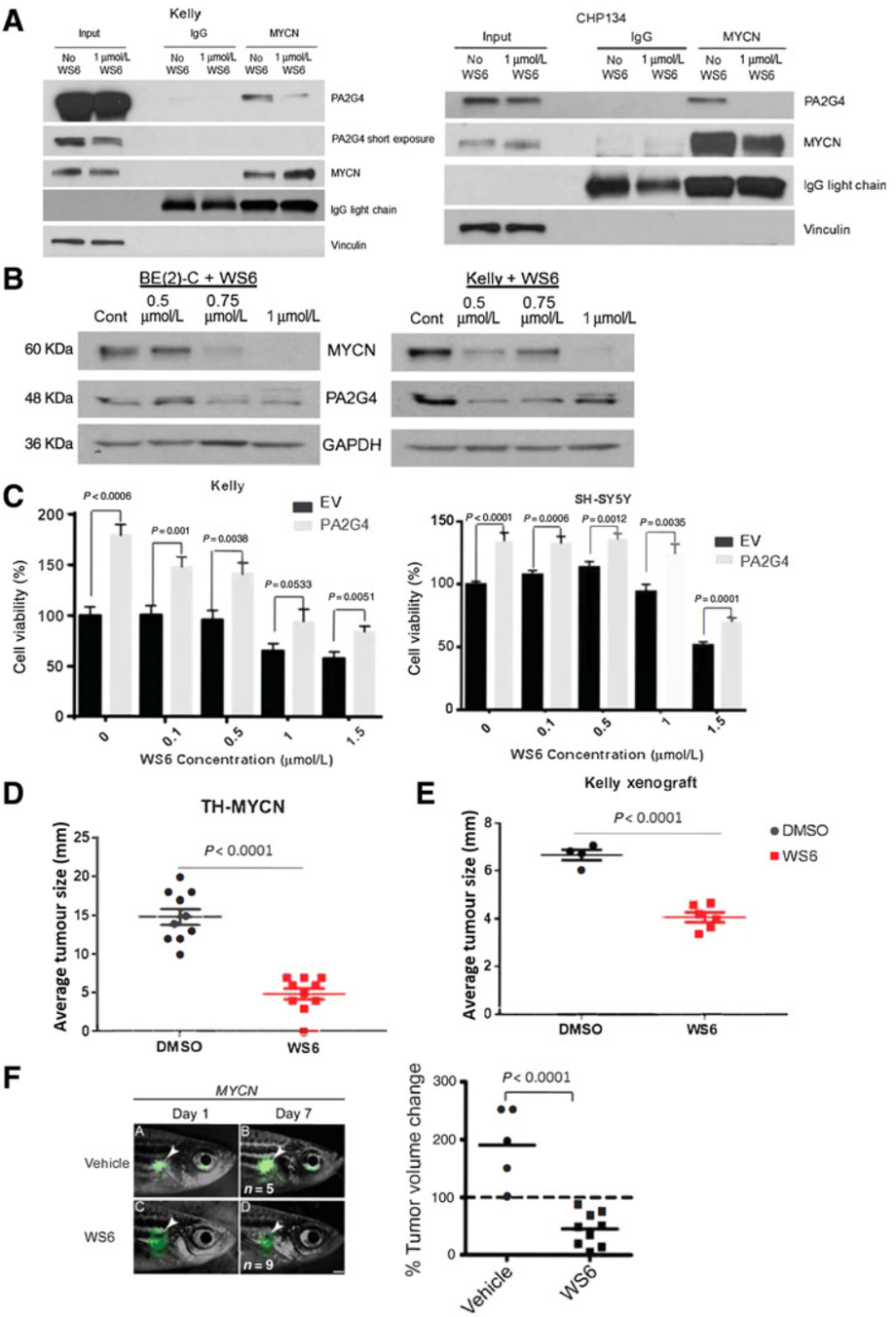

Figure 3.

Competitive chemical inhibition of MYCN-PA2G4 binding. **A,** Co-IP using IgG or anti-MYCN antibodies of total protein from Kelly and CHP-134 neuroblastoma cells, followed by immunoblotting with anti-PA2G4 or anti-MYCN antibodies. The neuroblastoma cells were treated with 1 μmol/L WS6 for 1 hour. **B,** Immunoblot of PA2G4, MYCN expression in BE(2)-C and Kelly cells treated with increasing concentrations of WS6 for 48 hours. **C,** Viability of SH-SY5Y and Kelly cells was measured by the Alamar Blue assay following transient transfection of empty vector (EV), or a PA2G4-MYC tag expression vector, followed by WS6 treatment at different concentrations for 48 hours. **D,** Abdominal neuroblastoma size among homozygous TH-*MYCN*$^{+/+}$ transgenic mice, either treated with DMSO or WS6. TH-*MYCN*$^{+/+}$ mice were treated with an intraperitoneal dose of 85 mg/kg/day for 5 of each 7 days from 3 weeks of age for 3 weeks or until the tumor reached 1,000 mm. **E,** Kelly cells were injected subcutaneously into the flank of BALB/c nude mice. When tumor size of 4 mm was formed, mice were treated with either DMSO or 70 mg/kg/day of WS6 for 5 consecutive days of each week for 3 weeks or until the tumor reached 1,000 mm. Each value shown in the figure represented data from four mice for DMSO and 6 mice for WS6. **F,** EGFP-expressing tumors (arrowhead) in the transgenic MYCN;GFP adult zebrafish, treated with either vehicle or WS6 at days 1 or 7 of treatment (left). Scale bar, 1 mm. Differences in tumor volume, as measured by the size of EGFP-positive tumor masses using ImageJ software, in zebrafish treated with vehicle or WS6 on day 7 versus day 1; mean values (horizontal bars) were compared by two-sample *t* test (right).

overexpression (SH-EP MYCN3, SH-EP-TRE-MYCN), increased PA2G4 expression and showed decreased MYC levels (Fig. 1C; Supplementary Fig. S1B and S1C). Whereas doxycycline-induced repression of MYCN expression in SHEP-tet21N neuroblastoma cells correlated with repressed PA2G4 and a reciprocal increase in MYC levels. The modest decrease in PA2G4 expression observed, despite the abrogation of MYCN, may be due to the reciprocal elevation of c-MYC levels. We performed ChIP assays and demonstrated a 4–10-fold enrichment of MYCN binding at canonical E-Box regulatory sequences situated within 500 bp upstream of the *PA2G4* TSS, and intron 1a and 1b of the *PA2G4* gene in two neuroblastoma cell lines (Fig. 1D; Supplementary Fig. S1D). MYCN chromatin binding was abolished by transiently transfected MYCN-specific siRNAs. These data indicate that MYCN enhances *PA2G4* gene transcription in neuroblastoma cells.

PA2G4 levels closely correlated with the high levels of MYCN protein expression across a panel of *MYCN*-amplified human

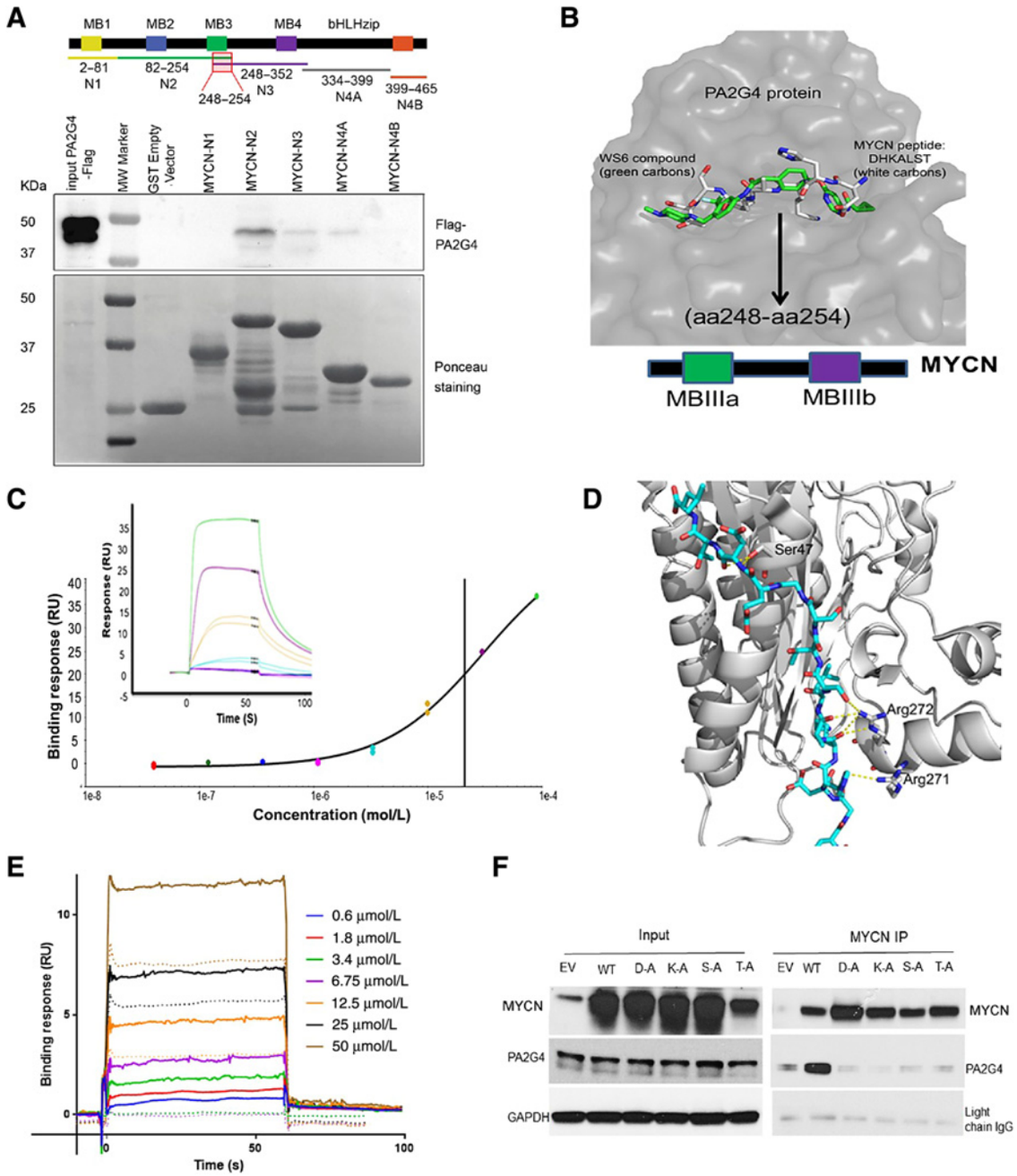

Figure 4.

Characterization of the PA2G4–MYCN protein–protein interface. **A,** GST pulldown of overexpressed GST-MYCN deletion mutant proteins and a *PA2G4*-3xFlag expression vector for 24 hours in HEK-293T cells, which were then immunoblotted with an anti-Flag antibody. **B,** Overlay of the independent representation of the docking solutions of WS6 (green carbons) and the MYCN oligopeptide DHKALST (white carbons) to PA2G4. Both were predicted to bind to the same surface pocket of PA2G4 (gray-filled space). **C,** A representative SPR (Biacore T200) experiment demonstrating a direct dose-response binding interaction between the bound PA2G4 exposed to increasing concentrations of the MYCN oligopeptide, DHKALST. Each experiment was run in duplicate. Overall this interaction had a calculated K_d of 28.3 ± 0.73 µmol/L ($n = 5$). **D,** A molecular model of the PA2G4–MYCN protein interface. The addition of two MYCN amino acids at the C-terminus and five at the N-terminus of the DHKALST MYCN oligopeptide resulted in an oligopeptide, GGDHKALSTGEDTL (cyan carbons), which interacted with PA2G4 (white carbons) in this molecular model. A visual analysis of this static dock predicted putative hydrogen bonds (yellow dashes) with residues Ser47, Arg271, and Arg272, which were subsequently targeted for mutagenesis. **E,** Representative SPR curves showing the concentration–response binding of DHKALST to PA2G4 (solid lines). The addition of 10 µmol/L WS6 resulted in a repression of this binding (dotted lines). This experiment was conducted in duplicate, three times. **F,** HEK293 cells were transiently transfected for 48 hours with MYCN wild-type (WT) or MYCN expression vector containing individual point mutants of the DHKALST region of MYCN to an alanine (D-A, K-A, S-A, and T-A). MYCN co-IP was performed, followed by immunoblotting with antibodies recognizing MYCN or PA2G4, and GAPDH. EV, empty vector.

neuroblastoma cell lines, but not in neuroblastoma cell lines that were nonamplified for *MYCN* (NBLS, SH-EP, and SK-N-FI; Supplementary Fig. S1E). Interestingly, two *MYCN* nonamplified cell lines, but with high MYC expression (SH-SY5Y and SK-N-AS), also had detectable levels of PA2G4, indicating a possible regulatory relationship between PA2G4 and MYC. Subcellular localization studies using immunoblotting of nuclear and cytoplasmic protein fractions from neuroblastoma cell lines and immunofluorescence showed that both MYCN and PA2G4 were colocalized in the nucleus (Supplementary Fig. S1F–S1H). Homozygous TH-*MYCN*$^{+/+}$ transgenic mice develop neuroblastoma in paravertebral and coeliac sympathetic ganglia at 6–7 weeks of age, after a precancer stage of neuroblast hyperplasia in the ganglia during the first 2 weeks of life (29). We found the PA2G4 expression pattern mirrored the high levels of MYCN produced by the *MYCN* transgene from neuroblastoma initiation in primary ganglia to later tumor formation (Supplementary Fig. S1I).

We next assessed whether PA2G4 participated in a positive feedforward expression loop with MYCN, as we have identified for other MYCN transactivation targets (7, 8, 30, 31). Following transient transfection of neuroblastoma cells with PA2G4-specific siRNAs, we found a marked reduction in both PA2G4 and MYCN protein (Fig. 2A), but not MYCN mRNA levels (Fig. 2B). Cycloheximide chase experiments assessing MYCN protein half-life demonstrated a 50% reduction following PA2G4 siRNA knockdown (Fig. 2C; Supplementary Fig. S2A), while PA2G4 overexpression caused a 2-fold increase in MYCN protein half-life (Fig. 2D; Supplementary Fig. S2B). The treatment of neuroblastoma cells with the proteasome inhibitor, MG132, resulted in increased MYCN protein levels, which were maintained at high levels even after PA2G4 knockdown, indicating that PA2G4 protects MYCN protein from ubiquitin-mediated proteasomal degradation (Fig. 2E). We next performed coimmunoprecipitation (co-IP) using a MYCN-specific antibody on neuroblastoma cell lysates after PA2G4 knockdown, and immunoblotted with an ubiquitin-specific antibody (Fig. 2F). Repression of PA2G4 expression was associated with an increase in MYCN ubiquitination. Studies in colorectal cancer cells suggested PA2G4 could bind directly to, and sequester Fbxw7 in the cytoplasm, thus indirectly increasing nuclear MYC protein stability (12). We investigated this potential mechanism of PA2G4 influencing MYCN protein stability indirectly by shifting the location of Fbxw7 toward the cytoplasm and possibly protecting nuclear proteins including MYCN. We measured nuclear and cytoplasmic Fbxw7 levels after modulating PA2G4 (Fig. 2G). We were unable to detect any change in Fbxw7 levels in the cytoplasm or nucleus in response to knocking down or overexpressing PA2G4, suggesting that PA2G4 is not involved in sequestering Fbxw7 to the cytoplasm in neuroblastoma cells. In-line with this, PA2G4 and Fbxw7 do not bind directly (Supplementary Fig. S2C). These findings are consistent with a model of PA2G4 directly binding to, and stabilizing MYCN, thereby protecting it from ubiquitin-mediated proteasomal degradation.

Table 1. The effect of PA2G4 on MYCN protein half-life

Plasmid DNA	Half-life (minutes)	*P*
Control EV	21.52 ± 0.18	
PA2G4	32.24 ± 2.84	0.028 (EV vs. PA2G4)
Mutant 1 (Ser47)	17.72 ± 2.40	0.022 (PA2G4 vs. Mutant 1)
Mutant 2 (Glu50)	24.17 ± 5.69	n.s (PA2G4 vs. Mutant 2)
Mutant 4 (Lys93)	27.18 ± 1.91	n.s (PA2G4 vs. Mutant 4)
Mutant 5 (Arg271)	19.31 ± 2.28	0.031 (PA2G4 vs. Mutant 5)
Mutant 6 (Arg272)	21.87 ± 1.68	0.047 (PA2G4 vs. Mutant 6)
Mutant 7 (Arg281)	26.65 ± 2.92	n.s (PA2G4 vs. Mutant 7)

NOTE: BE(2)-C cells were transiently transfected with either wild-type PA2G4, or six different PA2G4 point mutants at the PA2G4–MYCN protein–protein interface for 48 hours, then treated with 100 μg/μL cycloheximide for up to 60 minutes, followed by immunoblotting and densitometric analysis to measure the MYCN protein half-life.

Abbreviations: EV, empty vector; n.s, *P* value nonsignificant compared with wild-type PA2G4.

Table 2. Molecular dynamics simulations of comparative binding of the small seven amino acid MYCN peptide, DHKALST, and three mutant MYCN oligopeptides of this same sequence to PA2G4

MYCN peptide	Total energy (KJ/mol)	Extrapolated K_d (μmol/L)
DHKALST	−205,551 ± 2.2	28.3
DHAALST	−205,162 ± 2.7	125
DHKALAT	−204,764 ± 2.5	2,250
DHAALAT	−198,759 ± 3.0	2,600

NOTE: Total energy was calculated from the whole PA2G4:MYCN peptide complex after simulations. SPR was conducted on all these peptides against the wild-type PA2G4 protein and the extrapolated KDs were calculated using the BIAevaluation Software (GE Healthcare).

PA2G4 binds MYCN and chemical inhibition of binding reduces expression of both proteins and tumorigenicity

We hypothesized that the positive regulatory relationship between PA2G4 and MYCN expression may result from direct binding of PA2G4 to MYCN. We used co-IP to show that native PA2G4 directly bound native MYCN in two human *MYCN*-amplified neuroblastoma cell lines (Fig. 3A). A diarylamide-based compound, which binds PA2G4, WS6, had previously been identified in a screen for small molecules that stimulated pancreatic β islet cell growth (32). When we treated two human *MYCN*-amplified neuroblastoma cell lines with 1 μmol/L WS6 (Supplementary Fig. S3A) for only 1 hour, we showed that WS6 treatment completely blocked PA2G4-MYCN protein binding (Fig. 3A). Treatment of two *MYCN*-amplified neuroblastoma cell lines with 0.5–1 μmol/L WS6 reduced PA2G4 and MYCN expression levels (Fig. 3B), and decreased MYCN protein stability (Supplementary Fig. S3B). WS6 treatment of neuroblastoma cell lines reduced colony formation *in vitro* by 20-fold (Supplementary Fig. S3C). To determine the specificity of WS6 for PA2G4, we transfected and overexpressed PA2G4 in neuroblastoma cells, then treated the transfected cells with WS6. Overexpression of PA2G4 increased cell viability in the absence of WS6 and partially blocked the cytopathic effects of WS6, consistent with the hypothesis that the cytopathic effects of WS6 on neuroblastoma cells were caused in part by a reduction of PA2G4 levels (Fig. 3C; Supplementary Fig. S3D).

We next assessed the antitumor activity of WS6 in the homozygous TH-*MYCN*$^{+/+}$ mouse model of neuroblastoma. Mice with palpable intra-abdominal tumors at 3 weeks of age were treated with the MTD of 85 mg/kg WS6 intraperitoneally for 5 consecutive days per week for a maximum of 3 weeks, or until the tumor reached 1,000 mm. Treatment with WS6 caused a 2-fold reduction in tumor size and a corresponding decrease in MYCN and PA2G4 protein expression *in vivo* (Fig. 3D; Supplementary Fig. S3E). Moreover, athymic nude mice xenografted subcutaneously in the flank with MYCN-amplified Kelly neuroblastoma cells, then treated with the MTD of 70 mg/kg WS6 intraperitoneally for 5 consecutive days per week for a

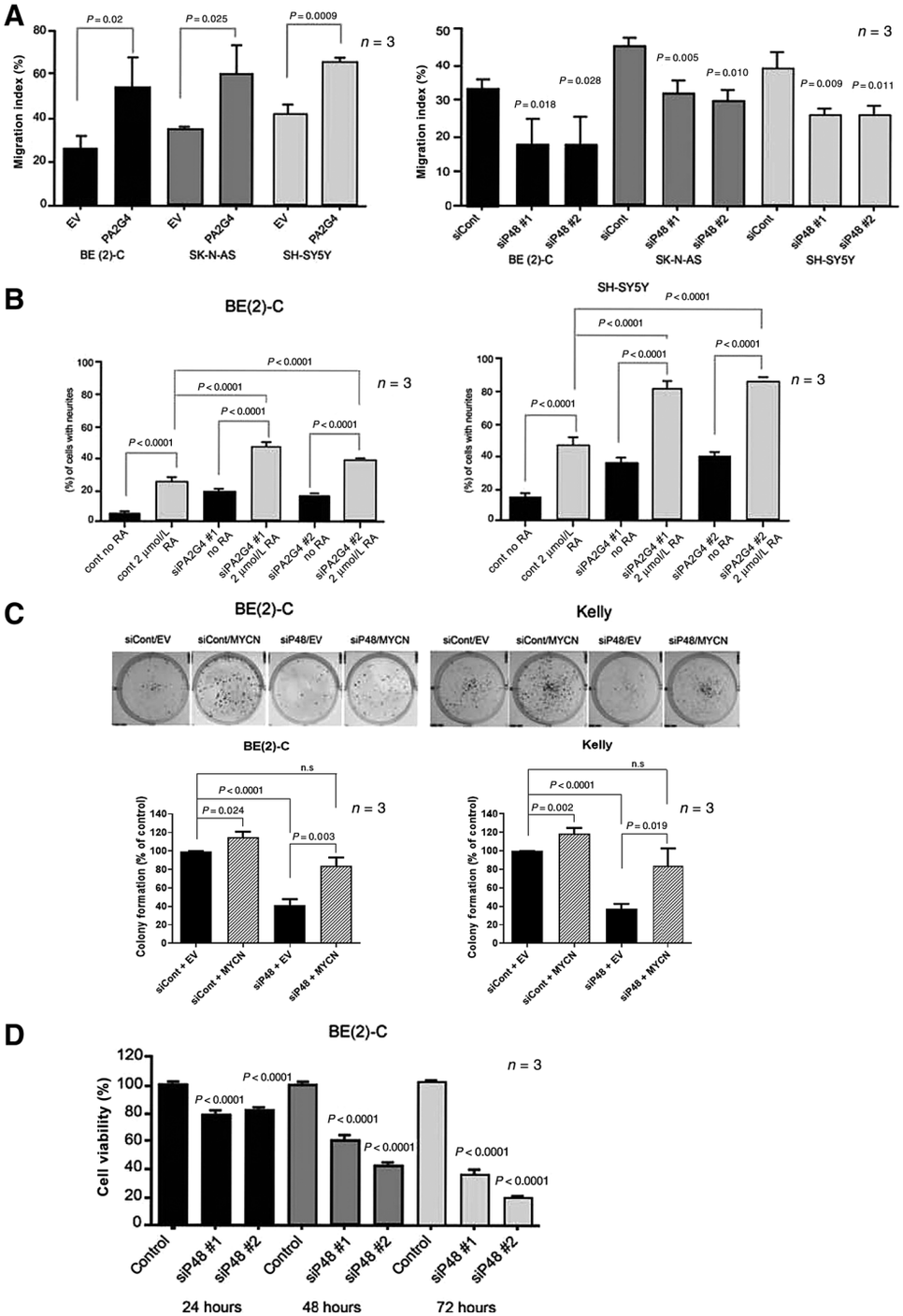

Figure 5.

PA2G4 expression enhances the malignant neuroblastoma phenotype *in vitro*. **A,** Migration index using the transwell migration assay for three neuroblastoma cell lines following either overexpression of PA2G4 or specific knockdown of the PA2G4 long isoform, p48. **B,** Neurite formation in BE(2)-C and SH-SY5Y cells transfected with PA2G4 siRNA and then treated with 2 µmol/L 13-cis-retinoic acid for 6 days. **C,** Colony formation assays for BE(2)-C and Kelly cells transfected with siRNA to the PA2G4 long isoform p48, or a concurrent transfection of the PA2G4 long isoform p48 and a *MYCN* expression vector. **D,** Cell viability measurements over 72 hours for BE(2)-C cells transfected with *PA2G4*-p48 siRNA. EV, empty vector; n.s, nonsignificant.

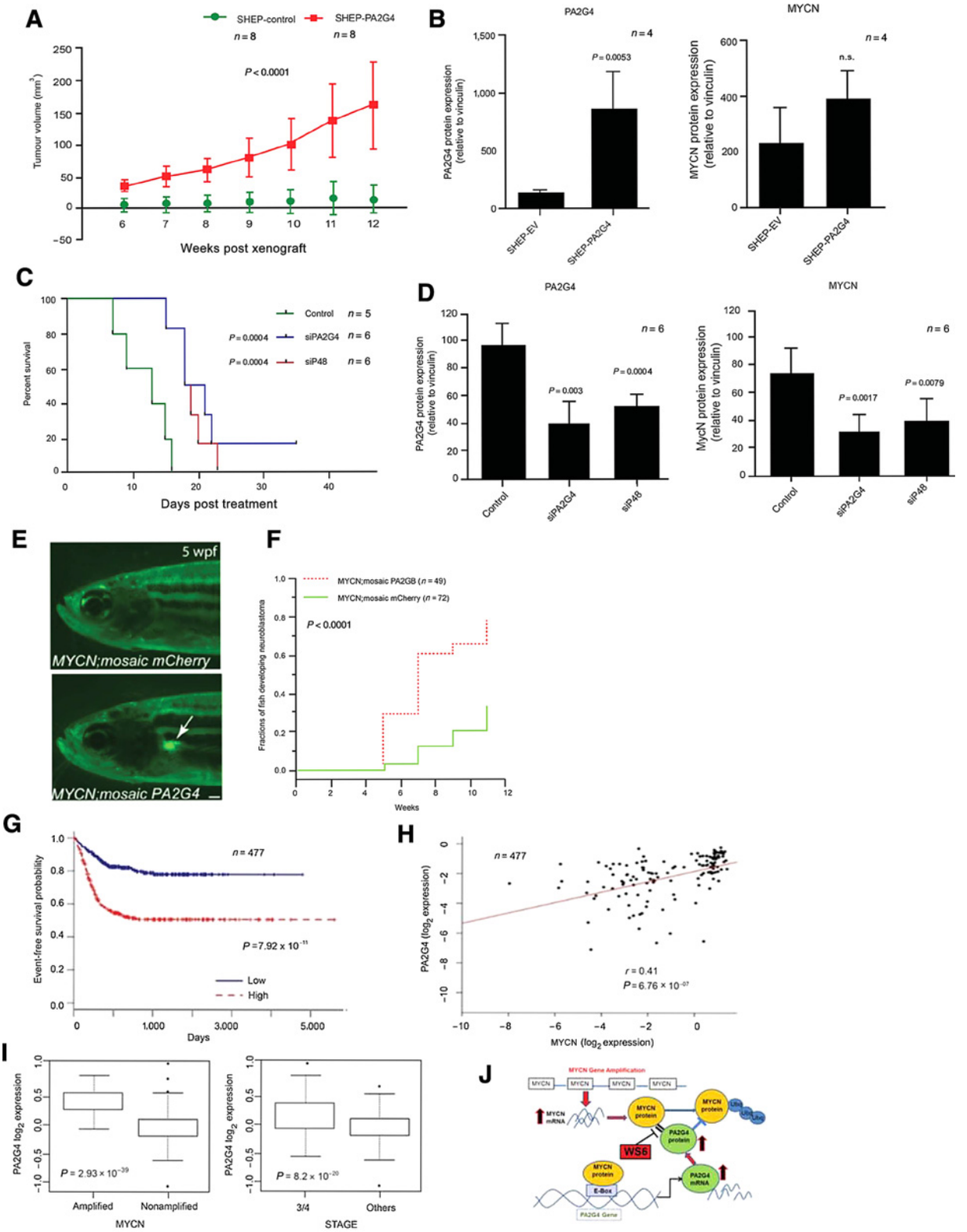

maximum of 3 weeks, also demonstrated an almost 2-fold reduction in tumor size (Fig. 3E). Adult MYCN transgenic zebrafish develop neuroblastoma in the inter-renal gland, an analog of the human adrenal gland (26). Intraperitoneal WS6 treatment of adult zebrafish with established neuroblastoma caused a 4-fold reduction in tumor size compared with solvent-treated controls and was accompanied by a marked reduction in PA2G4 and MYCN protein levels (Fig. 3F; Supplementary Fig. S3F).

To compare the relative potency of WS6 with other MYCN signal inhibitor molecules, we performed cytotoxicity treatment experiments *in vitro* against Kelly neuroblastoma cells and calculated IC_{50} values for the USP7 inhibitor, P22077 (33), the FACT inhibitor, CBL0137 (8), and the AurA kinase inhibitor, MLN8237. The IC_{50}s for the ATP-competitive Aurora-A inhibitor, CD532, against a range of tumor cell lines have been published previously (34). The IC_{50} comparisons (Supplementary Fig. S3G) showed WS6 had comparable single-agent potency to the USP7 inhibitor, the FACT inhibitor, and the ATP-competitive Aurora-A inhibitor, but not the AurA kinase inhibitor, which was more potent (35).

Characterization of the PA2G4–MYCN protein–protein interface

We next sought to better delineate the PA2G4–MYCN protein–protein interface. Using co-IP of transiently overexpressed GST-*MYCN* deletion mutant constructs and a full-length *PA2G4*-Flag vector in HEK-293T cells, we determined that the MYCN region bounds PA2G4. Only the MYCN deletion mutant consisting of amino acids 82–254 (MYCN-N2) bound strongly to PA2G4, while MYCN-N3 and -N4 had weak binding (Fig. 4A). Analysis of this MYCN region revealed a seven amino acid sequence (DHKALST, aa248–aa254) overlapping constructs MYCN-N2 and MYCN-N3, which was not repeated elsewhere in the MYCN protein. Computational molecular docking analysis of this MYCN oligopeptide (aa248–aa254) against the known PA2G4 crystal structure (36), predicted that this region of MYCN interacted with a specific surface pocket of PA2G4 (Fig. 4B). A blind dock across the whole surface of PA2G4 predicted that WS6 (in green) bound to PA2G4 at the same site as the seven amino acid MYCN oligopeptide. Furthermore, the modeling of an additional seven amino acids at the N- and C-termini suggested that this entire 14 amino acid MYCN sequence (aa246–aa259) contributed to binding.

To determine direct binding of these MYCN oligopeptides to PA2G4, we expressed and purified recombinant PA2G4 (aa9–aa394), then conducted SPR (Biacore T200) assays with the MYCN oligopeptides. Both the MYCN 7aa oligopeptide DHKALST (aa248–aa254) and the MYCN 14aa oligopeptide GGDHKALST-GEDTL (aa246–aa259) gave clear dose-response binding to immobilized PA2G4 with K_ds of 28.3 ± 0.73 μmol/L ($n = 5$) and 24.8 ± 0.61 μmol/L ($n = 5$), respectively (Fig. 4C). The molecular docking model further predicted PA2G4 amino acids Ser47, Glu50, Lys93, Arg271, Arg272, and Arg 281 were involved in hydrogen bonding with MYCN (Fig. 4D). When we compared the effect of transfected wild-type PA2G4 on MYCN protein half-life, to mutant PA2G4 at these seven sites, only transfected PA2G4 mutations at Ser47, Arg271, and Arg272 correlated with reduced MYCN stability (Fig. 4E; Supplementary Fig. S4A). Both the 7aa and 14aa MYCN oligopeptides also stabilized PA2G4 when measured by differential scanning fluorimetry (Supplementary Fig. S4B). Furthermore, where possible SPR experiments were conducted on the single mutants, giving extrapolated K_ds of 79.5 μmol/L and 175 μmol/L for the S47A and R272A mutations, respectively (Table 1; Supplementary Fig. S4C–S4E). SPR experiments showed that this triple mutant had an extrapolated K_d of >300 μmol/L (Supplementary Fig. S4D). Our molecular dynamics simulations suggested that MYCN amino acids Lys250 and Ser253 were involved in hydrogen bonds with PA2G4, for 3.2% and 18.8% of the simulation time, respectively. Equivalent molecular dynamics simulations with the MYCN oligopeptide residues mutated showed that MYCN oligopeptides DHAALST, DHKALAT, and DHAALAT were less energetically favorable than DHKALST, and SPR experiments showed each peptide had much higher extrapolated K_ds (Table 2). SPR competition experiments showed repression of MYCN oligopeptide DHKALST dose-response binding to immobilized PA2G4 when 10 μmol/L WS6 was preincubated with the MYCN oligopeptide, suggesting WS6 competed out the MYCN oligopeptide binding to PA2G4 (Fig. 4E). Next, we transiently transfected HEK293T cells with full-length wild-type MYCN or four individual point mutants of the DHKALST MYCN sequence, then performed co-IP with a MYCN antibody. Four individual amino acid mutations of MYCN-7aa sequence disrupted PA2G4 binding (Fig. 4F). Collectively, these data

Figure 6.

PA2G4 increases neuroblastoma tumorigenicity. **A,** Tumor xenograft volume measured weekly from 6–12 weeks post-injection, following flank inoculation into athymic nude mice of SHEP neuroblastoma cells, either stably overexpressing PA2G4 or an empty vector. *P* values were obtained using a two-way ANOVA multiple comparison test. **B,** Densitometric quantification of immunoblotted PA2G4 and MYCN protein expression in SH-EP tumor xenografts overexpressing PA2G4 or empty vector control tissues. n.s, *P* value nonsignificant compared with empty vector. **C,** Tumor growth in mice xenografted with BE(2)-C neuroblastoma cells, following direct injection of control or PA2G4 siRNA (40 μg) coupled with nanoparticles every 3 days for a total of eight injections, or until the tumor reached 1,000 mm. Survival comparisons were analyzed by a log-rank test. **D,** Protein densitometry of immunoblots of three tumor samples from each cohort showing the levels of PA2G4 and MYCN protein expression. Vinculin was used as a loading control, and each sample was normalized to control siRNA mouse. Data show means and SD derived from 6 mice per group. **E,** Fluorescence micrograph images of *MYCN* transgenic fish mosaically overexpressing mCherry alone (*MYCN*;mosaic mCherry; top) or *PA2G4* (*MYCN*;mosaic *PA2G4*; bottom). An EGFP-expressing tumor in the inter-renal gland (arrow) of *MYCN*;mosaic *PA2G4* transgenic fish at 5 weeks postfertilization (wpf; bottom). Scale bar, 0.5 mm. **F,** Kaplan–Meier analysis of the cumulative frequency of neuroblastoma induction over 11 weeks in the *MYCN*;mosaic mCherry and *MYCN*;mosaic *PA2G4* zebrafish lines ($P < 0.0001$). **G,** Kaplan–Meier plot for event-free survival of 477 patients with neuroblastoma from the Cologne dataset (R2 microarray analysis and visualization platform, http://r2.amc.nl) stratified by median primary tumor *PA2G4* expression level, $P = 7.92 \times 10^{-11}$. **H,** Correlation between *PA2G4* and *MYCN* mRNA expression for neuroblastoma tumors from the Cologne dataset, $r = 0.41$ and $P = 6.76 \times 10^{-7}$, $n = 477$. **I,** *PA2G4* mRNA expression level among 477 neuroblastoma tumors dichotomized by *MYCN* amplification status (nonamplified vs. amplified; $P = 2.93 \times 10^{-39}$) or clinical stage (advanced stage: 3, 4 vs. other stages: 1, 2, 4S; $P = 8.2 \times 10^{-20}$). **J,** A hypothetical model of the oncogenic function of PA2G4 in *MYCN*-driven neuroblastoma. MYCN amplification leads to high MYCN mRNA and protein levels. MYCN protein then binds the PA2G4 gene promoter and stimulates PA2G4 transcription. The consequently higher levels of PA2G4 protein directly binds MYCN, protecting it from ubiquitin-mediated degradation, thus ensuring a feedforward expression loop that is essential for maintaining high levels of both proteins. WS6 competitively disrupts the PA2G4-MYCN–binding site, leading to a marked reduction in the levels of both proteins.

suggest that PA2G4 binds a 14aa MYCN sequence (aa246–aa259) through PA2G4 amino acid residues Ser47, Arg271, and Arg272, reducing MYCN ubiquitination and thus increasing its stability.

PA2G4 drives the malignant neuroblastoma phenotype *in vitro* and *in vivo*

We demonstrated strong causal relationships between PA2G4 expression and other features of the malignant phenotype of neuroblastoma cells *in vitro*. Overexpression of PA2G4-p48 in neuroblastoma cells increased cell migration in the transwell migration assay, whereas PA2G4-p48 knockdown had the converse effect (Fig. 5A). Neuroblastoma cells are arrested in the pathway toward neuritic differentiation, which can be restored *in vitro* by treatment with 13-*cis*-retinoic acid, an agent used in treatment of the disease (37). Knockdown of PA2G4 increased the sensitivity of neuroblastoma cell lines to the neurite-forming effects of 13-*cis*-retinoic acid (Fig. 5B; Supplementary Fig. S5A) and markedly reduced *in vitro* colony formation (Fig. 5C). Cotransfected *MYCN* restored the effect of PA2G4 knockdown on neuroblastoma cell colony formation.

The *PA2G4* gene transcribes two alternatively spliced mRNA isoforms encoding proteins of 48 and 42 kDa, which have been previously reported to behave, respectively, as an oncoprotein or a tumor suppressor protein in cancer cells (16, 17, 19, 38). Immunoblotting with a PA2G4 antibody demonstrated that both PA2G4-p48 and -p42 were expressed in neuroblastoma cells (Supplementary Fig. S5B). The knockdown of the PA2G4-p48 isoform reduced viability of *MYCN*-amplified neuroblastoma cell lines (Fig. 5D; Supplementary Fig. S5C). Whereas overexpression of PA2G4-p48 increased cell proliferation and viability, regardless of *MYCN* amplification status, in five neuroblastoma cell lines, but not in normal fibroblast cells (Supplementary Fig. S5D–S5F). In neuroblastoma cells, we found that PA2G4-p42 also acted as an oncoprotein, because overexpression of PA2G4-p42 increased both cell growth and colony formation (Supplementary Fig. S5G and S5H). Thus, both PA2G4 isoforms increased the malignant phenotype of neuroblastoma cells *in vitro*.

To assess the effect of PA2G4 on neuroblastoma tumorigenicity *in vivo*, we first used SH-EP neuroblastoma cells, which had no *MYCN* amplification or PA2G4 expression. SH-EP cells stably transfected with an empty vector (EV) control (SH-EP-EV) or a PA2G4 expression vector (SH-EP-PA2G4) were mixed with Matrigel and injected subcutaneously into the dorsal flank of athymic nude mice. SH-EP-PA2G4 cells were tumorigenic, whereas SH-EP-EV cells were not (Fig. 6A; Supplementary Fig. S6A and S6B). Excised tumor tissues from these mice exhibited increased PA2G4 protein and mRNA expression, but MYCN protein expression increases did not reach statistical significance (Fig. 6B; Supplementary Fig. S6C and S6D). We next used self-assembling cationic star polymers (39) mixed with siRNA as an *in vivo* nanoparticle delivery system targeting either total PA2G4, PA2G4-p48, or scrambled control, to assess the effect of inhibiting PA2G4 by direct injection of PA2G4 siRNA into established PA2G4-expressing neuroblastoma tumors. Tumor latency was significantly delayed in mice carrying xenografts injected with siRNA targeting total PA2G4 or PA2G4-p48 (Fig. 6C). Immunoblotting of protein lysates from excised residual tumor tissues for PA2G4 and MYCN expression demonstrated a decrease in expression of both proteins *in vivo* (Fig. 6D; Supplementary Fig. S6E). Significant decreases in PA2G4 and MYCN mRNA expression were also observed for both PA2G4 and PA2G4-p48 siRNA-treated tumors, compared with control siRNA-treated tumors (Supplementary Fig. S6F), confirming that the PA2G4-MYCN codependency signal is a significant driver of neuroblastoma tumorigenesis *in vivo*.

To assess the significance of PA2G4 and MYCN overexpression on neuroblastoma pathogenesis in another species, we transiently overexpressed a PA2G4 construct in the peripheral sympathetic nervous system under the control of the *dβh* promoter in Tg(dβh:*EGFP-MYCN*) transgenic zebrafish. A *dbh-mCherry* construct was transiently overexpressed in the *MYCN* transgenic fish to serve as a control for this experiment. We identified *EGFP*-positive masses at 5 weeks of age in the inter-renal gland of transgenic fish mosaically overexpressing PA2G4 (Fig. 6E). By 11 weeks of age, 79% of *MYCN* transgenic fish mosaically overexpressing PA2G4 had tumors (Fig. 6F), a rate much higher than in the *MYCN* fish mosaically overexpressing *mCherry* (32.5%; $P < 0.0001$). Taken together these results indicate that PA2G4 is a potent oncogenic cofactor for *MYCN*-driven neuroblastoma tumorigenesis across different species.

PA2G4 is an oncogenic driver in human MYCN-driven cancer

High mRNA expression of PA2G4 had a strong association with poor neuroblastoma patient prognosis in a publicly available R2 gene expression database ($n = 477$; Cologne dataset) of primary neuroblastoma samples (Fig. 6G; Supplementary Fig. S6G and S6H; refs. 40, 41). We also found a correlation between high PA2G4 mRNA expression and MYCN amplification in a second cohort of primary neuroblastoma samples using real-time PCR ($n = 40$, Sydney Children's Hospital; Supplementary Fig. S6I). High *PA2G4* mRNA expression in the Cologne dataset correlated with MYCN expression, particularly in *MYCN*-amplified tumor tissues (Fig. 6H). Univariate comparisons showed that PA2G4 expression was higher in patients with other known predictors of poor prognosis, such as advanced clinical stage (3/4) and *MYCN* amplification (Fig. 6I). Multivariate analysis showed that high PA2G4 expression retained independent prognostic significance, when PA2G4 was compared with other prognostic factors in neuroblastoma (Supplementary Fig. S6J).

We next sought evidence of this association in other human *MYCN*-driven tumorigenesis. Publically available data from The Cancer Genome Atlas revealed a high frequency of *PA2G4* amplification (16%) in the *MYCN*-driven human neuroendocrine prostate cancer (NEPC; Supplementary Fig. S6K; ref. 42), indicating PA2G4 may also be a driver in this malignancy. Together these data suggest that PA2G4 is an oncogenic cofactor in *MYCN*-driven human cancer, and, that there is a functional interdependency between MYCN and PA2G4.

Discussion

Here we have identified a novel MYCN-binding protein, PA2G4, which protects MYCN from ubiquitin-mediated proteolysis in neuroblastoma cells. MYCN acts in a forward feedback expression loop with PA2G4, driving ever higher levels of each protein and consequently oncogenesis (Fig. 6J). This same regulatory relationship for PA2G4 and MYCN may extend to other human cancer types, such as NEPC. Surprisingly, this forward feedback regulatory relationship even operated in

neuroblastoma cells with amplified *MYCN*, suggesting that strong oncoprotein instability barriers must exist in normal cells to prevent transformation by MYCN, making MYCN stability an attractive drug target.

PA2G4 was originally identified as a cell-cycle–regulated protein (human homolog of the mouse protein p38-2AG4) and then an ErbB3-binding protein (43, 44). Subsequent studies showed that PA2G4 belongs to a family of DNA/RNA binding proteins implicated in cell growth, apoptosis, and differentiation (45). The longer PA2G4 isoform, p48 (375 amino acids), was ubiquitously expressed in the cytoplasm and nucleus, and suppressed apoptosis (15). PA2G4-p48 has a known oncogenic function via a direct interaction with nuclear histone deacetylases causing transcriptional repression of tumor suppressor genes with effects on cell-cycle regulation and ribosomal synthesis (15, 16, 46). PA2G4-p48 overexpression in glioblastoma cells enhanced tumor growth in mouse xenograft models and contributed to oral tumorigenesis by activating podoplanin expression (21). Our data strongly supports the role of PA2G4 as an oncogene in *MYCN*-driven neuroblastoma in humans, mice, and zebrafish. However, PA2G4 may have MYCN-dependent and -independent oncogenic effects, as suggested by our finding that high PA2G4 expression in neuroblastoma tumor tissue had prognostic significance, which was independent of *MYCN* amplification. While our studies indicated nuclear and cytoplasmic PA2G4 expression in neuroblastoma cells, it will be important to assess whether PA2G4–MYCN complexes can bind DNA and directly influence transcription. Moreover, other proteins may also bind in this complex influencing MYCN stability, so that the comparative potency of the PA2G4-MYCN mechanism of maintaining MYCN stability to other MYCN stability factors needs to be determined (6–8, 30, 31, 33, 47–49).

Our structural analyses indicated that PA2G4 exhibited high affinity binding to a short amino acid MYCN sequence at MYC Box IIIb (aa246–259), protecting MYCN from proteasomal degradation. In combination with computational molecular dynamics, mutagenesis of both the PA2G4 protein and MYCN oligopeptides highlighted the important amino acids that give significant energy contributions to this protein–protein interface. This site is physically quite distinct from the well described phosphodegron within MYC Box I (aa 58–62) where the E3 ligase, Fbxw7, binds to direct MYC and MYCN toward proteasomal degradation in normal and malignant cells (6), but overlaps another putative MYC phosphodegron (aa 242–250) and *MYC* mutational hotspot in human lymphoma (50). Whether PA2G4 can interact directly or indirectly with other regions of MYCN, MYC, or other phosphodegron binding proteins such as AurA or Fbxw7, is unknown. Our studies indicate that WS6 directly competes with MYCN binding to PA2G4, thus, it is possible that WS6 will exhibit favorable synergy with inhibitors of AurA or other compounds affecting MYCN stability.

We have defined the amino acids responsible for PA2G4-MYCN binding, and show that this binding site can be competitively blocked with significant antitumor effects *in vivo*. Our findings have important implications for the design of anti-MYCN therapeutics. We saw no ill-effects in TH-*MYCN* or xenografted mice treated with WS6. WS6 displayed therapeutic effects, however, the compound itself is not drug-like, but it serves as a very useful positive control and chemical tool for future drug discovery campaigns targeting PA2G4. PA2G4 and MYCN expression levels were very low in normal fibroblasts. Moreover, PA2G4 expression in these normal cells affected neither cell proliferation nor viability, suggesting inhibitors of PA2G4 may have low toxicity in normal tissues. Loss of PA2G4 in knockout mice caused only mildly reduced fecundity and early growth, but adult mice appeared normal (51). In contrast, our experiments showed that WS6 caused significant cytopathic effects *in vitro* and *in vivo* in neuroblastoma cell lines and tissues, which correlated with reductions in MYCN and PA2G4 levels. The cytopathic action of WS6 in neuroblastoma cells was blocked by exogenous overexpression of PA2G4, indicating specificity for the target. The interaction between the MYCN amino acid sequence, GGDHKALSTGEDTL, and a pronounced surface crevice in PA2G4 defined by residues Ser47, Glu50, Lys93, Arg271, Arg272, and Arg281, represents a novel protein–protein interface for future anti-MYCN drug design. Small-molecule drug discovery projects aimed at large, flat, featureless protein surfaces for, what may be, transient protein–protein interactions have previously been seen as very challenging. However, multiple recent successes in the discovery and development phases of protein–protein interface inhibitor design, and the progress of several of these compounds into successful clinical trials, indicate that these problems can now be overcome (5). The IC_{50} for WS6 in treated neuroblastoma cells was a relatively high average of 650 nmol/L; however, as a tool inhibitor compound, WS6 can provide the basis for medicinal chemistry and optimization for clinical use in future. Our data points to the exciting prospect of a novel MYCN signal inhibitor with WS6 properties, which competitively blocks PA2G4-MYCN binding and markedly lowers the level of both proteins, providing a completely new focus for the design of MYCN inhibitors.

Disclosure of Potential Conflicts of Interest

M. Fischer has received speakers bureau honoraria from Janssen-Cilag and Novartis. No potential conflicts of interest were disclosed by the other authors.

Authors' Contributions

Conception and design: J. Koach, J.K. Holien, H. Massudi, G. Milazzo, J.E. Murray, G. Perini, M.W. Parker, B.B. Cheung, G.M. Marshall

Development of methodology: J. Koach, J.K. Holien, H. Massudi, O.C. Ciampa, M. Herath, G. Milazzo, J.A. McCarroll, L. Doughty, B.B. Cheung

Acquisition of data (provided animals, acquired and managed patients, provided facilities, etc.): J. Koach, J.K. Holien, D.R. Carter, O.C. Ciampa, M. Herath, T. Lim, G. Milazzo, J.E. Murray, J.A. McCarroll, B. Keenan, B.W. Stevenson, M.A. Gorman, J.L. Bell, L. Doughty, S. Hüttelmaier, A. Oberthuer, M. Fischer, X. Zhang, S. Zhu, W.C. Gustafson, G.M. Marshall

Analysis and interpretation of data (e.g., statistical analysis, biostatistics, computational analysis): J. Koach, J.K. Holien, H. Massudi, O.C. Ciampa, M. Herath, T. Lim, J.A. Seneviratne, G. Milazzo, J.A. McCarroll, B. Liu, C. Mayoh, B. Keenan, B.W. Stevenson, J.L. Bell, L. Doughty, A. Oberthuer, A.J. Gifford, T. Liu, S. Zhu, G. Perini, M.W. Parker, B.B. Cheung, G.M. Marshall

Writing, review, and/or revision of the manuscript: J. Koach, J.K. Holien, H. Massudi, D.R. Carter, O.C. Ciampa, J.E. Murray, J.A. McCarroll, M.A. Gorman, L. Doughty, A. Oberthuer, M. Fischer, W.C. Gustafson, M. Haber, M.D. Norris, J.I. Fletcher, M.W. Parker, B.B. Cheung, G.M. Marshall

Administrative, technical, or material support (i.e., reporting or organizing data, constructing databases): J. Koach, J.K. Holien, O.C. Ciampa, J.A. Seneviratne, L. Doughty

Study supervision: J.K. Holien, S. Zhu, J.I. Fletcher, M.W. Parker, B.B. Cheung, G.M. Marshall

Other (interpretation of histopathologic data): A.J. Gifford

Acknowledgments

This work was supported by Program Grants (to G.M. Marshall, M.D. Norris, and Michelle Haber) from the National Health and Medical Research Council

(NHMRC) Australia (APP1016699), Cancer Institute NSW (10/TPG/1-13), Cancer Council NSW (PG-11-06), and an Australia Postgraduate Research Award, UNSW Sydney, Australia (to J. Koach). This work was also supported by NHMRC Project grant APP1125171 and Neuroblastoma Australia (to G.M. Marshall and B.B. Cheung); Project grant APP571073; Senior Principal Research Fellowship to M.W. Parker, Cure Cancer Australia Foundation, Leukemia Foundation, and 5-point Foundation (Postdoctoral Fellowships to J.K. Holien). Infrastructure support from the NHMRC Independent Research Institutes Infrastructure Support Scheme and the Victorian State Government Operational Infrastructure Support Program to St Vincent's Institute is gratefully acknowledged. The authors thank the Sydney Children's Tumour Bank Network for providing samples and related clinical information for this study.

The costs of publication of this article were defrayed in part by the payment of page charges. This article must therefore be hereby marked *advertisement* in accordance with 18 U.S.C. Section 1734 solely to indicate this fact.

Received April 5, 2019; revised July 17, 2019; accepted September 3, 2019; published first September 9, 2019.

References

1. Park JR, Bagatell R, London WB, Maris JM, Cohn SL, Mattay KK, et al. Children's Oncology Group's 2013 blueprint for research: neuroblastoma. Pediatr Blood Cancer 2013;60:985–93.
2. Brodeur GM. Neuroblastoma: biological insights into a clinical enigma. Nat Rev Cancer 2003;3:203–16.
3. Weiss WA, Aldape K, Mohapatra G, Feuerstein BG, Bishop JM. Targeted expression of MYCN causes neuroblastoma in transgenic mice. EMBO J 1997;16:2985–95.
4. Marshall GM, Carter DR, Cheung BB, Liu T, Mateos MK, Meyerowitz JG, et al. The prenatal origins of cancer. Nat Rev Cancer 2014;14:277–89.
5. Nero TL, Morton CJ, Holien JK, Wielens J, Parker MW. Oncogenic protein interfaces: small molecules, big challenges. Nat Rev Cancer 2014;14: 248–62.
6. Otto T, Horn S, Brockmann M, Eilers U, Schuttrumpf L, Popov N, et al. Stabilization of N-Myc is a critical function of Aurora A in human neuroblastoma. Cancer Cell 2009;15:67–78.
7. Marshall GM, Liu PY, Gherardi S, Scarlett CJ, Bedalov A, Xu N, et al. SIRT1 promotes N-Myc oncogenesis through a positive feedback loop involving the effects of MKP3 and ERK on N-Myc protein stability. PLoS Genet 2011; 7:e1002135.
8. Carter DR, Murray J, Cheung BB, Gamble L, Koach J, Tsang J, et al. Therapeutic targeting of the MYC signal by inhibition of histone chaperone FACT in neuroblastoma. Sci Transl Med 2015;7:312ra176.
9. Welcker M, Orian A, Jin J, Grim JE, Harper JW, Eisenman RN, et al. The Fbw7 tumor suppressor regulates glycogen synthase kinase 3 phosphorylation-dependent c-Myc protein degradation. Proc Natl Acad Sci U S A 2004;101:9085–90.
10. Richards MW, Burgess SG, Poon E, Carstensen A, Eilers M, Chesler L, et al. Structural basis of N-Myc binding by Aurora-A and its destabilization by kinase inhibitors. Proc Natl Acad Sci U S A 2016;113:13726–31.
11. Xiao D, Yue M, Su H, Ren P, Jiang J, Li F, et al. Polo-like Kinase-1 regulates Myc stabilization and activates a feedforward circuit promoting tumor cell survival. Mol Cell 2016;64:493–506.
12. Wang Y, Zhang P, Wang Y, Zhan P, Liu C, Mao JH, et al. Distinct interactions of EBP1 isoforms with FBXW7 elicits different functions in cancer. Cancer Res 2017;77:1983–96.
13. Figeac N, Serralbo O, Marcelle C, Zammit PS. ErbB3 binding protein-1 (Ebp1) controls proliferation and myogenic differentiation of muscle stem cells. Dev Biol 2014;386:135–51.
14. Neilson KM, Abbruzzesse G, Kenyon K, Bartolo V, Krohn P, Alfandari D, et al. Pa2G4 is a novel Six1 co-factor that is required for neural crest and otic development. Dev Biol 2017;421:171–82.
15. Liu Z, Ahn JY, Liu X, Ye K. Ebp1 isoforms distinctively regulate cell survival and differentiation. Proc Natl Acad Sci U S A 2006;103:10917–22.
16. Kim CK, Nguyen TL, Joo KM, Nam DH, Park J, Lee KH, et al. Negative regulation of p53 by the long isoform of ErbB3 binding protein Ebp1 in brain tumors. Cancer Res 2010;70:9730–41.
17. Ko HR, Nguyen TL, Kim CK, Park Y, Lee KH, Ahn JY. P42 Ebp1 functions as a tumor suppressor in non-small cell lung cancer. BMB Rep 2015;48: 159–65.
18. Ahn JY, Liu X, Liu Z, Pereira L, Cheng D, Peng J, et al. Nuclear Akt associates with PKC-phosphorylated Ebp1, preventing DNA fragmentation by inhibition of caspase-activated DNase. EMBO J 2006;25:2083–95.
19. Kim CK, Lee SB, Nguyen TL, Lee KH, Um SH, Kim J, et al. Long isoform of ErbB3 binding protein, p48, mediates protein kinase B/Akt-dependent HDM2 stabilization and nuclear localization. Exp Cell Res 2012;318: 136–43.
20. Liu Z, Oh SM, Okada M, Liu X, Cheng D, Peng J, et al. Human BRE1 is an E3 ubiquitin ligase for Ebp1 tumor suppressor. Mol Biol Cell 2009;20: 757–68.
21. Mei Y, Zhang P, Zuo H, Clark D, Xia R, Li J, et al. Ebp1 activates podoplanin expression and contributes to oral tumorigenesis. Oncogene 2014;33: 3839–50.
22. Zeid R, Lawlor MA, Poon E, Reyes JM, Fulciniti M, Lopez MA, et al. Enhancer invasion shapes MYCN-dependent transcriptional amplification in neuroblastoma. Nat Genet 2018;50:515–23.
23. Bolger AM, Lohse M, Usadel B. Trimmomatic: a flexible trimmer for Illumina sequence data. Bioinformatics 2014;30:2114–20.
24. Ambrosini G, Groux R, Bucher P. PWMScan: a fast tool for scanning entire genomes with a position-specific weight matrix. Bioinformatics 2018;34: 2483–4.
25. Zhang X, Dong Z, Zhang C, Ung CY, He S, Tao T, et al. Critical role for GAB2 in neuroblastoma pathogenesis through the promotion of SHP2/MYCN cooperation. Cell Rep 2017;18:2932–42.
26. Zhu S, Lee JS, Guo F, Shin J, Perez-Atayde AR, Kutok JL, et al. Activated ALK collaborates with MYCN in neuroblastoma pathogenesis. Cancer Cell 2012;21:362–73.
27. Phillips JC, Braun R, Wang W, Gumbart J, Tajkhorshid E, Villa E, et al. Scalable molecular dynamics with NAMD. J Comput Chem 2005;26: 1781–802.
28. Humphrey W, Dalke A, Schulten K. VMD: visual molecular dynamics. J Mol Graph 1996;14:33–8.
29. Hansford LM, Thomas WD, Keating JM, Burkhart CA, Peaston AE, Norris MD, et al. Mechanisms of embryonal tumor initiation: distinct roles for MycN expression and MYCN amplification. Proc Natl Acad Sci U S A 2004; 101:12664–9.
30. Liu PY, Xu N, Malyukova A, Scarlett CJ, Sun YT, Zhang XD, et al. The histone deacetylase SIRT2 stabilizes Myc oncoproteins. Cell Death Differ 2013;20: 503–14.
31. Sun Y, Liu PY, Scarlett CJ, Malyukova A, Liu B, Marshall GM, et al. Histone deacetylase 5 blocks neuroblastoma cell differentiation by interacting with N-Myc. Oncogene 2014;33:2987–94.
32. Shen W, Tremblay MS, Deshmukh VA, Wang W, Filippi CM, Harb G, et al. Small-molecule inducer of beta cell proliferation identified by high-throughput screening. J Am Chem Soc 2013;135:1669–72.
33. Tavana O, Li D, Dai C, Lopez G, Banerjee D, Kon N, et al. HAUSP deubiquitinates and stabilizes N-Myc in neuroblastoma. Nat Med 2016; 22:1180–6.
34. Gustafson WC, Meyerowitz JG, Nekritz EA, Chen J, Benes C, Charron E, et al. Drugging MYCN through an allosteric transition in Aurora kinase A. Cancer Cell 2014;26:414–27.
35. Mosse YP, Lipsitz E, Fox E, Teachey DT, Maris JM, Weigel B, et al. Pediatric phase I trial and pharmacokinetic study of MLN8237, an investigational oral selective small-molecule inhibitor of Aurora kinase A: a Children's Oncology Group Phase I Consortium study. Clin Cancer Res 2012;18: 6058–64.
36. Kowalinski E, Bange G, Bradatsch B, Hurt E, Wild K, Sinning I. The crystal structure of Ebp1 reveals a methionine aminopeptidase fold as binding platform for multiple interactions. FEBS Lett 2007;581:4450–4.
37. Matthay KK, Reynolds CP, Seeger RC, Shimada H, Adkins ES, Haas-Kogan D, et al. Long-term results for children with high-risk neuroblastoma treated on a randomized trial of myeloablative therapy followed by 13-cis-retinoic acid: a children's oncology group study. J Clin Oncol 2009;27: 1007–13.

38. Ko HR, Kim CK, Lee SB, Song J, Lee KH, Kim KK, et al. P42 Ebp1 regulates the proteasomal degradation of the p85 regulatory subunit of PI3K by recruiting a chaperone-E3 ligase complex HSP70/CHIP. Cell Death Dis 2014;5:e1131.
39. Teo J, McCarroll JA, Boyer C, Youkhana J, Sagnella SM, Duong HT, et al. A rationally optimized nanoparticle system for the delivery of RNA interference therapeutics into pancreatic tumors *in vivo*. Biomacromolecules 2016;17:2337–51.
40. Oberthuer A, Hero B, Berthold F, Juraeva D, Faldum A, Kahlert Y, et al. Prognostic impact of gene expression-based classification for neuroblastoma. J Clin Oncol 2010;28:3506–15.
41. Kocak H, Ackermann S, Hero B, Kahlert Y, Oberthuer A, Juraeva D, et al. Hox-C9 activates the intrinsic pathway of apoptosis and is associated with spontaneous regression in neuroblastoma. Cell Death Dis 2013;4:e586.
42. Carver BS. Defining and targeting the oncogenic drivers of neuroendocrine prostate cancer. Cancer Cell 2016;29:431–2.
43. Radomski N, Jost E. Molecular cloning of a murine cDNA encoding a novel protein, p38-2G4, which varies with the cell cycle. Exp Cell Res 1995;220: 434–45.
44. Lessor TJ, Hamburger AW. Regulation of the ErbB3 binding protein Ebp1 by protein kinase C. Mol Cell Endocrinol 2001;175:185–91.
45. Miao X, Tang Q, Miao X, Wu Y, Qian J, Zhao W, et al. ErbB3 binding protein 1 (EBP1) participates in the regulation of intestinal inflammation via mediating Akt signaling pathway. Mol Immunol 2015;67:540–51.
46. Zhang Y, Hamburger AW. Specificity and heregulin regulation of Ebp1 (ErbB3 binding protein 1) mediated repression of androgen receptor signalling. Br J Cancer 2005;92:140–6.
47. Liu T, Liu PY, Marshall GM. The critical role of the class III histone deacetylase SIRT1 in cancer. Cancer Res 2009;69:1702–5.
48. Marshall GM, Gherardi S, Xu N, Neiron Z, Trahair T, Scarlett CJ, et al. Transcriptional upregulation of histone deacetylase 2 promotes Myc-induced oncogenic effects. Oncogene 2010;29:5957–68.
49. Shahbazi J, Scarlett CJ, Norris MD, Liu B, Haber M, Tee AE, et al. Histone deacetylase 2 and N-Myc reduce p53 protein phosphorylation at serine 46 by repressing gene transcription of tumor protein 53-induced nuclear protein 1. Oncotarget 2014;5:4257–68.
50. Chakraborty AA, Scuoppo C, Dey S, Thomas LR, Lorey SL, Lowe SW, et al. A common functional consequence of tumor-derived mutations within c-MYC. Oncogene 2015;34:2406–9.
51. Zhang Y, Lu Y, Zhou H, Lee M, Liu Z, Hassel BA, et al. Alterations in cell growth and signaling in ErbB3 binding protein-1 (Ebp1) deficient mice. BMC Cell Biol 2008;9:69.